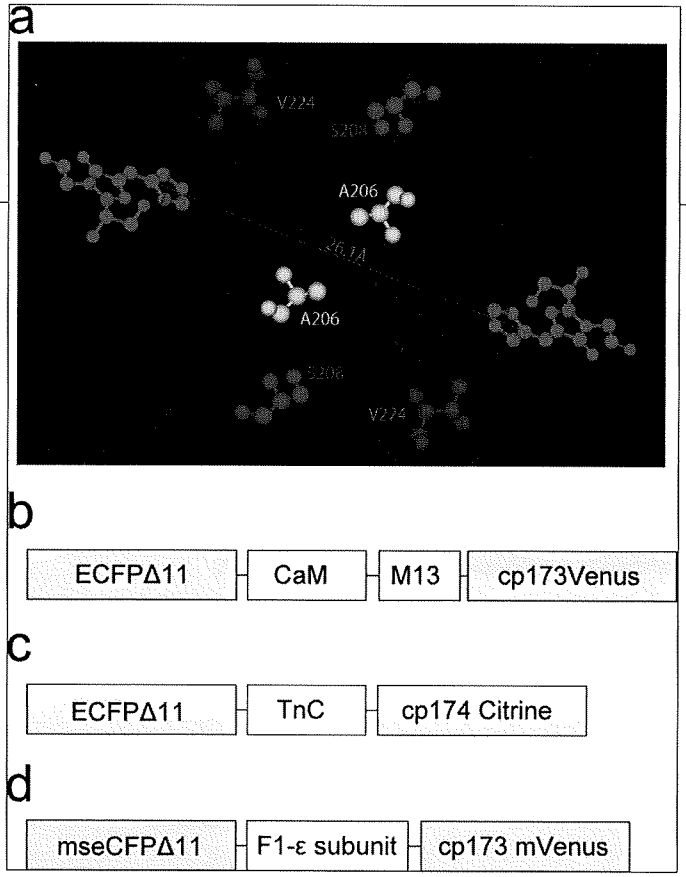

Figure 1. a) Relative orientation of the essential amino acid residues at the dimer interface of the *Aequorea* GFPs. A206 residues are shown in yellow, S208 in red, and V224 in blue. The chromophores are in green, and the green line indicates the distance between the chromophores, which is calculated to be ~26 Å (*9*). Schematic representation of the FRET-based indicators analyzed in this study: b) cameleon YC3.60, c) TN-XL, and d) ATeam.

prove the dynamic range of the indicator, adjustment of the linkers between the domains (*4*) and optimization of the dipole orientation by using circularly permuted FPs (*5*) are routine.

In addition to these techniques, a pair of cyan- and yellow-FP variants, CyPet and YPet (*6*), respectively, was developed as an optimized FRET pair through a directed-evolution process. A protease indicator containing this FP pair showed a 20-fold change in the emission ratio upon cleavage of the linker peptide between CyPet and YPet, whereas only a 4-fold change was observed when conventional enhanced cyan-FP (ECFP) and enhanced yellow-FP (EYFP) were used. This increase in the dynamic range observed for CyPet and YPet was attributed to the enhanced dimerization of these FPs by substituting serine at 208 and valine at 224 for phenylalanine (S208F) and leucine (V224L), respectively (*7*), that are present at the dimer interface (*8, 9*) (Figure 1, panel a). Moreover, it was reported that utilizing ECFP/YPet pair in some FRET-based indicators also increases the dynamic range of the indicators (*10*). On the other hand, monomeric FPs, which are made by substituting alanine at 206 for lysine (A206K) (*11*), are also widely accepted to be used as the FRET donor and acceptor (*12*), because the formation of *Aequorea* FP dimers at high concentration (dissociation constant (K_d) = 110 μM) (*11*) can induce artifactual FRET due to oligomerization of the FPs in the indicators. One report suggests that A206K mutation leads to a better dynamic range (*13*), while another report suggests the mutation almost abolishes the FRET signal (*14*). Thus, it is currently unclear how desirable FP dimerization is for the construction of FRET-based indicators.

To date, there have been no reports systematically examining the effect of the FP dimerization on the performance of FRET-based indicators in terms of the dynamic range of the signal change and the FRET efficiency. Here, we systematically compared the relationship between the dimerization property of the *Aequorea* FPs and the performance of FRET-based indicators. Our results using FP variants with no, weak, or enhanced dimerization revealed that FPs with a weak dimerization property yielded efficient indicators with the greatest dynamic range of signal change.

RESULTS AND DISCUSSION

Comparison of the Dynamic Range Using YC3.60 Dimer Mutants *in Vitro*. To investigate the effect of the FP dimerization ability on the properties of FRET-based indicators, we first analyzed the effect of the A206K mutation in the *Aequorea* FPs of the Ca^{2+} indicator, yellow cameleon variant YC3.60 (*5*). We mutated the original YC3.60 (Figure 1, panel b) with a native dimerization interface (YC3.60-nD/nA) to place the monomer-associated A206K on the donor FP (YC3.60-mD/nA), the acceptor FP (YC3.60-nD/mA), or both the donor and acceptor (YC3.60-mD/mA) FPs. In the absence of Ca^{2+}, no obvious spectroscopic difference was observed among the recombinant YC3.60 variants (dotted curve, Figure 2, panels a–d). When Ca^{2+} was added, however, the YFP/CFP ratio was decreased among the A206K mutants (solid curves, Figure 2, panel b–d). The greatest reduction in the YFP/CFP ratio was observed using the YC3.60-mD/mA mutant (solid curve, Figure 2, panel d). The dynamic range of the emission intensity change in the indicator was calculated for each variant (Table 1). In accordance with previous findings (*5*), the dynamic range of YC3.60-nD/nA reached 557%, whereas the ranges observed with the YC3.60-nD/mA and YC3.60-

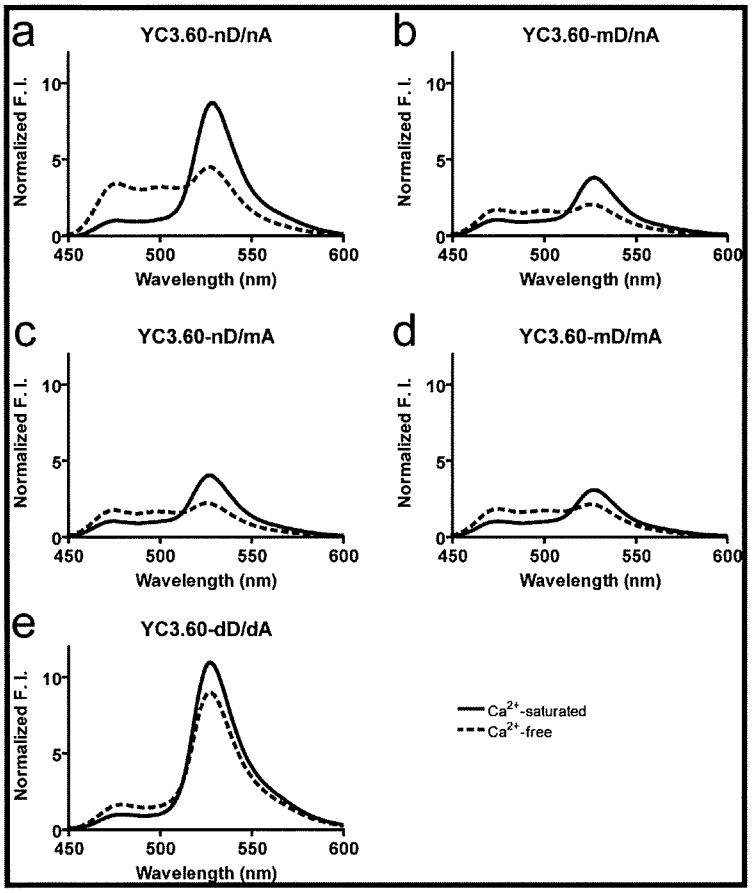

Figure 2. Fluorescence spectra of cameleon YC3.60 variants. a) The original cameleon YC3.60-nD/nA. Variants with monomer-associated mutants b) YC3.60-mD/nA, c) YC3.60-nD/mA, and d) YC3.60-mD/mA and e) with the dimer-enhanced mutant YC3.60-dD/dA in Ca^{2+}-saturated (solid curves) and Ca^{2+}-free (dotted curves) buffer. The spectra are normalized to the CFP peak in Ca^{2+}-saturated buffer. F.I. = fluorescence intensity.

TABLE 1. Dynamic range (DR) and YFP/CFP ratio of the FRET signal change in FRET-based indicators

	nD/nA			mD/nA			nD/mA			mD/mA			dD/dA		
	YFP/CFP ratio			YFP/CFP ratio			YFP/CFP ratio			YFP/CFP ratio			YFP/CFP ratio		
	DR, %	Ca^{2+}-satd	Ca^{2+}-free	DR, %	Ca^{2+}-satd	Ca^{2+}-free	DR, %	Ca^{2+}-satd	Ca^{2+}-free	DR, %	Ca^{2+}-satd	Ca^{2+}-free	DR, %	Ca^{2+}-satd	Ca^{2+}-free
YC3.60	554	8.6	1.3	208	3.8	1.2	212	4.1	1.3	159	3.1	1.2	100	11.0	5.5
TN-XL	460	3.8	0.7	278	2.6	0.7	283	2.5	0.6	229	2.2	0.7	84	3.9	2.1
ATeam	128	3.7	1.6	100	2.9	1.5	103	2.3	1.1	90	2.5	1.3	85	4.8	2.6

mD/nA mutants were less than half that level. The YC3.60-mD/mA mutant further reduced the dynamic range of the indicator to 159%. These results suggest that introducing the monomer-associated mutation into

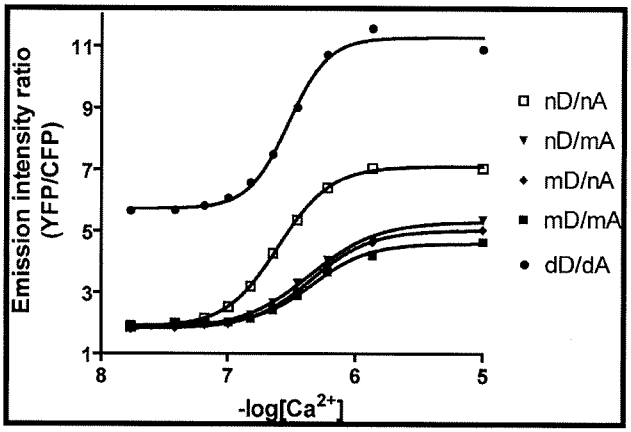

Figure 3. Ca^{2+} titration of the recombinant YC3.60 dimerization variants. The recombinant proteins were mixed with various concentrations of Ca^{2+}, and the YFP/CFP emission intensity ratios were measured and plotted as a function of $-\log[Ca^{2+}]$.

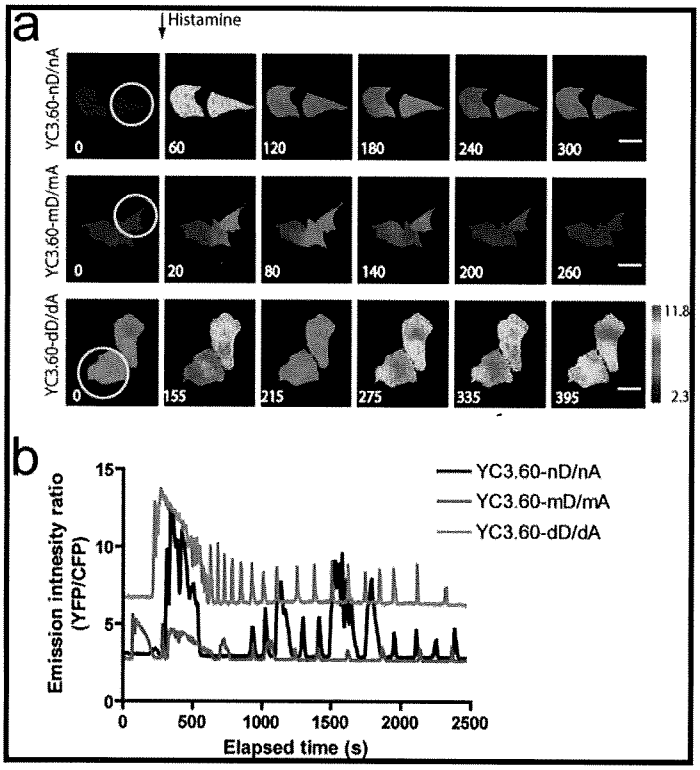

Figure 4. Ca^{2+} imaging in living cells by using YC3.60 with dimer interface mutations. a) A series of pseudocolored images of HeLa cells that expressed YC3.60-nD/nA (top row), YC3.60-mD/mA (middle row), and YC3.60-dD/dA (bottom row). Circles in the left panel of each row indicate the regions of interest for measuring the FRET signals. Scale bar, 10 μm. b) Time course of the YFP/CFP emission ratios after the addition of 20 μM histamine. The time scale is the time after the histamine addition.

the FPs reduces the FRET efficiency and also the dynamic range of the indicator.

In contrast, the dimerization-inducing S208F/V224L mutations have been reported to enhance both the FRET efficiency and the dynamic range of a protease indicator (*7*). Therefore, we next examined the effect of introducing the S208F/V224L dimer-enhancing mutations into the FPs of cameleon (YC3.60-dD/dA). In contrast to the results with the A206K mutants, the S208F/V224L mutants of YC3.60-dD/dA showed a YFP/CFP ratio similar to that of the original YC3.60-nD/nA when Ca^{2+} was added to the solution (solid curve, Figure 2, panel e). However, when Ca^{2+} was excluded from the indicator solution, little reduction in the YFP/CFP ratio was observed (dotted curve, Figure 2, panel e), indicating that some portion of the donor and acceptor were still in contact owing to the enhanced dimerization. As a result, the overall dynamic range of YC3.60-dD/dA was reduced more than 5 times, to 100% (Table 1).

These results suggested that dimerization of the FPs does not always improve the performance of FRET-based indicators. We speculated that the discrepancy with the previous results using a protease indicator (*6, 7*) were due to the difference in the mechanism of the indicators. Unlike YC3.60, the substrate domain of the protease indicator is irreversibly cleaved between the donor and acceptor, permanently separating them. Once the donor and acceptor are physically disconnected, the dimerization characteristics of the FPs minimally affect the FRET signal if the concentration of the cleaved FPs is lower than the dissociation constant. Thus, a strong tendency for the FPs to undergo dimerization is desirable in the case of protease indicators, because it enhances the FRET signal before the cleavage, while it minimally affects the cleaved FPs. In contrast, change in the FRET signal of YC3.60 is caused by a reversible reaction, *i.e.*, the intramolecular distance between the donor and acceptor reversibly changes upon Ca^{2+} binding and release. In constructing such indicators, the design plan must maintain the delicate balance of the conformational equilibrium within the indicator. Either overdimerization or overmonomerization of the FPs would restrict the dynamic range of the indicators.

To investigate the effects of dimerization interface mutations on the Ca^{2+}-sensing domains of YC3.60, we performed Ca^{2+} titration assays and analyzed the affinity of the YC3.60 variants for Ca^{2+} (Figure 3, Supplementary Table 1). The K_d value of the original YC3.60

(YC3.60-nD/nA) was 249 nM, which is comparable to its previously reported value (*5*), whereas that of the YC3.60 variants with monomer-associated mutations was about 2-fold higher (approximately 450 nM). Among them, YC3.60-mD/mA showed the lowest affinity for Ca^{2+} (K_d = 465 nM). In contrast, the K_d value of the YC3.60 with dimeric FPs (YC3.60-dD/dA) was 298 nM, which was similar to the value for the original YC3.60 (Figure 3, Supplementary Table 1). These results suggest that the monomer-associated mutation in the FPs causes the donor and acceptor to repel, which in turn affects the interaction between Ca^{2+}-calmodulin and the calmodulin-binding M13 peptide in the indicator, lowering the Ca^{2+} affinity of the sensor domain.

It was reported previously that GFPs dimerize in antiparallel configuration, at least in the crystal (*9*). In YC3.60, the Venus moiety has been circularly permutated so that Venus has been turned upside down relative to the ECFP moiety. We hypothesized that the high FRET efficiency of YC3.60 was caused by the circular permutation not because of the relative orientation of chromophore dipoles but because of the dimerization of the FPs in antiparallel configuration. To obtain deeper insight, we analyzed the effect of the mutations in indicators whose donor and acceptor cannot assume antiparallel configuration. As expected, the monomeric mutations had minimum effect on YC3.12 and YC3.30 (Supplementary Figure 1), both of which have ECFP and Venus moieties connected on the same side of the barrel with short linkers (*5*). Nevertheless, the dimeric mutations did increase the FRET efficiency of the indicators both in Ca^{2+}-free and Ca^{2+}-saturated condition. Considering the molecular structure of these indicators and the fact that the dynamic range is actually reduced, intermolecular dimerization may have caused such increase in FRET efficiency.

Comparison of the Dynamic Range of YC3.60 Containing FP Dimer Mutants in Live Cells. We next measured the indicator performance in live cells expressing the YC3.60 variants. HeLa cells were treated with 20 μM histamine, a condition that induces a large Ca^{2+} response in live mammalian cells, enabling the indicators to be adequately saturated with Ca^{2+} (Figure 4, panel a). By measuring the fluorescence intensity ratios of the donor and acceptor FPs, we could roughly estimate the dynamic range of the indicators in living cells. YC3.60-mD/mA displayed a reduced fluorescence intensity ratio at the peak (Figure 4, panel b). Furthermore, the baseline ratio of YC3.60-dD/dA was clearly higher than that of the other YC3.60 variants, although the peak ratio after histamine stimulation was comparable to that of YC3.60-nD/nA. These results in live cells were in good agreement with the results of our *in vitro* spectroscopic assays described above and further confirmed the importance of dimer interface optimization in FRET-based reversible indicators.

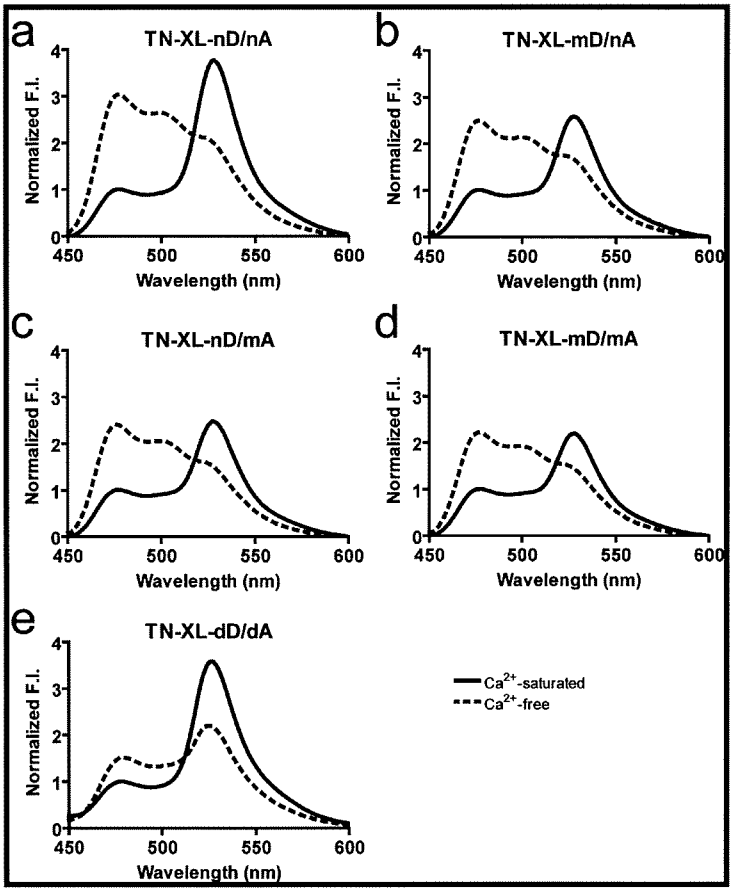

Figure 5. Fluorescence spectra of cameleon TN-XL variants. a) Original TN-XL (TN-XL-nD/nA), b) TN-XL-mD/nA, c) TN-XL-nD/mA, d) TN-XL-mD/mA, and e) TN-XL-dD/dA in Ca^{2+}-saturated (solid curves) and Ca^{2+}-free (dotted curves) buffer. The spectra are normalized to the CFP peak measured in Ca^{2+}-saturated buffer. F.I. = fluorescence intensity.

Effect of Dimer Interface Mutations in Another FRET-Based Indicator, TN-XL. To fortify our hypothesis, we analyzed the effects of dimerization interface mutations on the properties of another FRET-based Ca^{2+} indicator, TN-XL (*15*) (Figure 1, panel c), which uses the same

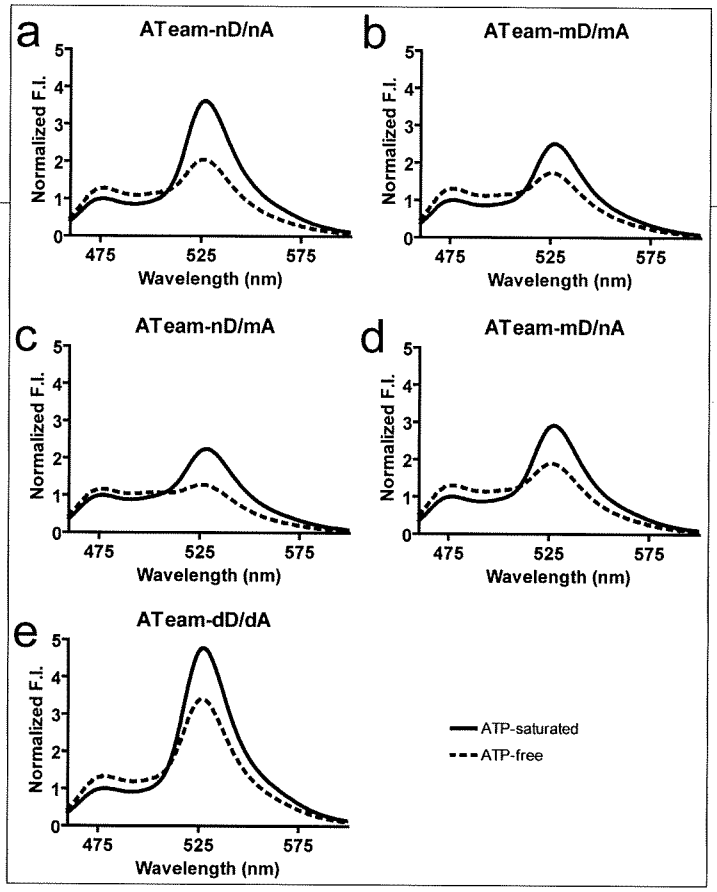

Figure 6. Fluorescence spectra of ATeam variants. a) The improved ATeam-nD/nA. Variants with monomer-associated mutants b) ATeam-mD/nA, c) ATeam-nD/mA, and d) the original ATeam-mD/mA and e) with the dimer-enhanced mutant ATeam-dD/dA in 10 mM ATP (solid curves) and ATP-free (dotted curves) buffer. The spectra are normalized to the CFP peak measured in 10 mM ATP buffer. F.I. = fluorescence intensity.

Aequorea FPs as YC3.60 but differs in its Ca^{2+}-sensing domain, which is troponin instead of calmodulin. The TN-XL was affected by the interface mutations in a manner essentially identical to YC3.60: the YFP/CFP ratio was decreased when Ca^{2+} was added to TN-XL with the A206K mutation on the donor (TN-XL-mD/nA), acceptor (TN-XL-nD/mA), and both the donor and acceptor (TN-XL-mD/mA) FPs, and the YFP/CFP ratio was increased in the TN-XL with the S208F/V224L mutations (TN-XL-dD/dA) when Ca^{2+} was omitted (Figure 5, Table 1).

Improvement of the Performance of the ATP Indicator ATeam by Dimer Interface Optimization. To generalize our hypothesis, we next sought to improve the performance of a FRET-based indicator that already has a wide dynamic range, by optimizing the dimerization interface. ATeam, a recently developed ATP indicator (*16*)(Figure 1, panel d), has a molecular configuration similar to that of YC3.60, in which the ε subunit of the bacterial F_oF_1-ATP synthase, used as an ATP-sensing domain, is sandwiched between *Aequorea* FPs. Upon binding ATP, ATeam undergoes conformational changes that generate a higher FRET signal by decreasing the distance between the donor and acceptor.

Like many other genetically encoded FRET-based indicators, the original ATeam has the monomer-associated A206K mutation in both its acceptor and donor FPs (*i.e.*, ATeam-mD/mA). However, an ATeam containing the native K206A FP variant (ATeam-nD/nA) showed a YFP/CFP ratio higher than that of the original ATeam (ATeam-mD/mA) when ATP was added, whereas the YFP/CFP emission ratios of both ATeam-nD/nA and ATeam-mD/mA in the absence of ATP were almost identical. Dimeric ATeam (ATeam-dD/dA), as in the case of Ca^{2+} indicators mentioned above, showed greatly reduced dynamic range due to high baseline level in the ATP-unbound form (Figure 6, Table 1). Thus, we increased the YFP/CFP ratio by changing the lysine at 206 back to alanine, achieving a 40% gain in ATeam's dynamic range.

We then compared the dynamic range of the ATeam variants in living HeLa cells. To deplete ATP, the cells were cultured in galactose medium and treated with oligomycin A, an inhibitor of F_oF_1-ATP synthase. Before oligomycin A addition, the ATeam-nD/nA-expressing cells showed an intensity ratio larger than that of cells expressing the original ATeam (ATeam-mD/mA). However, upon ATP depletion, the intensity ratio of both indicators decreased to a comparable value, indicating that ATeam-nD/nA had a higher dynamic range in living cells (Figure 7).

Conclusions and Outlook. Here we demonstrated that the monomer-inducing mutation in *Aequorea* FPs, which disrupts the dimer interface through introduced positive charges, reduces the FRET efficiency of reversible FRET-based indicators. We also found that the dimer-enhancing mutations S208F and V224L also reduced the dynamic range of the indicators by increasing the basal FRET efficiency, possibly due to the formation of intermolecular dimerization. These observations were in contrast to results obtained using a protease indicator, whose overall performance was improved by enhancing the dimerization property of the FPs (*6, 7*). The difference seems to depend on whether the signal-inducing reaction of the indicator is reversible or irreversible. For reversible FRET-based indicators, the balance between the enhancement of dimerization and the maintenance of free dissociation is critical. Taking advantage of these observations, we improved the dynamic range of a FRET-based ATP indicator

by changing the lysine at 206 in the FPs back to alanine.

To construct high-performance FRET-based indicators that reversibly show a large change in the FRET signal, the FPs should have a moderate dimeric property, to enable conformational change in the indicator's sensor domain and yet prevent undesired interactions between the FPs, for efficient FRET. Among the *Aequorea* FP variants we examined, those with alanine at 206 most closely matched these requirements, although a better interface might be obtainable, which should be examined in future studies. Our present recommendation is to examine possible combinations of mutations at the interface empirically and to screen for the highest dynamic range in each case. Until more data are available for predicting the results of such mutations, such screening for the optimal interface is essential.

One thing to note for the design of efficient FRET-based indicators is the relative orientation of the FPs. In order for the FPs to dimerize, they have to be bound in antiparallel configuration. Because wildtype GFP has both N- and C-termini in close proximity, simple fusion of FPs with a short linker will not result in antiparallel dimerization of FP moieties. This fact might explain why circularly permutated FPs are so effective in increasing the FRET efficiency in many indicators: it turns the FP upside down for antiparallel configuration. Although we have shown some evidence to support such notion, the details need to be clarified in future studies.

Our hypothesis might also explain the fact that, despite theoretical competence and many experimental trials, no non-*Aequorea* FRET pairs with high FRET efficiency have been found to date (*17–19*), whereas the FRET efficiency of some *Aequorea* FRET pairs approaches unity (*20*). It would be interesting to examine whether interface engineering can be applied to improve the performance of FRET pairs that use non-*Aequorea* FPs with longer absorption and emission wavelengths, for which a larger Förster distance is expected by theory, thereby expanding the applicability of this technique.

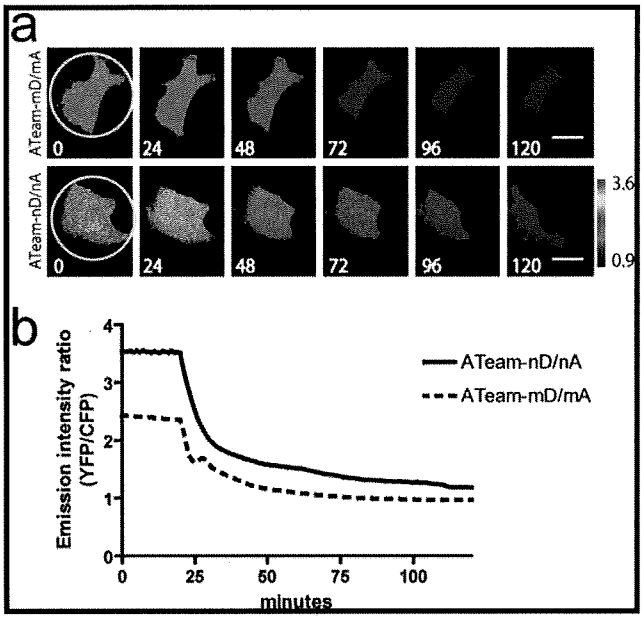

Figure 7. ATP imaging in living cells by using ATeam with dimer interface mutations. a) A series of pseudocolored images of HeLa cells that expressed the original ATeam (ATeam-mD/mA) (top row) and improved ATeam-nD/nA (bottom row). Cells cultured in galactose medium were treated with 10 μg mL^{-1} oligomycin A to deplete the intracellular ATP. Circles in the left panel of each row indicate the regions of interest for the FRET-signal measurements. Scale bar, 10 μm. b) Time course of the YFP/CFP emission ratios after the addition of oligomycin A.

METHODS

Generation of Mutant Indicators. Mutations were introduced by a modified version of QuikChange (Stratagene), to generate multiple mutations with a single cloning step (*21*). Intervector subclonings were performed using FASTR, an automatic cloning technology, as described previously (*22*). Briefly, the insert and vector fragments were amplified by PCR (KOD-plus, Toyobo) according to the manufacturer's protocol. The PCR conditions were as follows: 94 °C/2 min, (94 °C/15 s, 60 °C/30 s, 68 °C/90 s) 35 cycles, 68 °C /5 min. One microliter of the PCR solution from each sample was transferred to a mixture containing the following reagents in a total volume of 20 μL: 17 mM Tris-acetate, 25 mM Tris-HCl (pH 7.5), 5 mM $MgCl_2$, 5 mM magnesium acetate, 33 mM potassium acetate, 5 mM ATP, 5 mM DTT, 63 μg mL^{-1} BSA, 5 U of LguI (Fermentas), 400 U of T4 DNA ligase (New England Biolabs), 20 U of DpnI (NEB), and 5 mM aphidicolin (Calbiochem). The mixture was incubated without agitation at RT for 1 h. After incubation, 5 μL of the mixture was used to transform *E. coli* (XL10Gold, Stratagene).

Protein Expression, *in Vitro* Spectroscopy, and Ca^{2+} Titrations. Recombinant YC3.60, TN-XL, and ATeam protein variants with N-terminal polyhistidine tags were expressed in *Escherichia coli* [JM109(DE3)] at RT and purified using a Ni-NTA column (Qiagen) followed by buffer exchange to PBS(−) with an Amicon YM10 centrifugal filter (Millipore). Fluorescent spectra were measured with an F-2500 fluorescence spectrophotometer (Hitachi). Upon excitation with 430-nm light, the emission spectra of 0.3 μM recombinant cameleon were obtained using the

F-2500 fluorescence spectrophotometer (Hitachi). Ca^{2+} titrations were performed by the reciprocal dilution of Ca^{2+}-saturated and Ca^{2+}-free buffers containing MOPS (10 mM), KCl (100 mM), and EGTA (10 mM) with or without $CaCl_2$ (10 mM) at pH 7.2, RT. The free Ca^{2+} was calculated using 151 nM as the K_d value of EGTA for Ca^{2+}. The averaged data from three independent measurements was fitted to the Hill equation in a two-site model using GraphPad Prism (GraphPad Software).

Cell Culture, Transfection, and Imaging. HeLa cells were grown in Dulbecco's modified Eagle's medium (DMEM) containing 10% heat-inactivated FCS. The cells were transfected with expression vectors encoding various FRET-based indicators by using SuperFect (Qiagen), and cultured in phenol-red-free DMEM. One day after transfection, the cells were subjected to imaging. Wide-field observations of the cells were performed on a Nikon Ti inverted microscope (Nikon Instruments) using a PlanApo VC60, 1.40 numerical aperture (NA), oil-immersion objective (Nikon). Filters used for the dual-emission ratio imaging of YC3.60 and ATeam were purchased from Semrock: an FF01-427/10 excitation filter, an FF458-Di01 dichroic mirror, and two emission filters (FF01-483/32 for CFP and FF01-542/27 for YFP). The two emission filters were alternated by using a filter changer (Nikon). The cells were illuminated using a 100 W mercury lamp through 12.5% and 25% neutral density filters. The fluorescence emission from the indicators was imaged using a cooled charge-coupled device (CCD) camera (ORCA-AG; Hamamatsu Photonics); the exposure times were 500 ms for the CFP and YFP images. The cells were maintained on the microscope at 37 °C with a continuous supply of 95% air and 5% carbon dioxide by using a stage-top incubator (Tokai Hit). Image analysis was performed using Aquacosmos (Hamamatsu Photonics).

Acknowledgment: The authors thank O. Griesbeck for providing the TN-XL. This work was partly supported by Grant-in-Aid for Young Scientists (A) of Japan Society for the Promotion of Science, and Scientific Research on Advanced Medical Technology of the Ministry of Labor, Health and Welfare of Japan.

Supporting Information Available: This material is available free of charge *via* the Internet at http://pubs.acs.org.

REFERENCES

1. Miyawaki, A., *et al.* (1997) Fluorescent indicators for Ca^{2+} based on green fluorescent proteins and calmodulin, *Nature 388*, 882–887.
2. Stryer, L. (1978) Fluorescence energy transfer as a spectroscopic ruler, *Annu. Rev. Biochem. 47*, 819–846.
3. Tsien, R.-Y. (1998) The green fluorescent protein, *Annu. Rev. Biochem. 67*, 509–544.
4. Nagai, T., and Miyawaki, A. (2004) A high-throughput method for development of FRET-based indicators for proteolysis, *Biochem. Biophys. Res. Commun. 319*, 72–77.
5. Nagai, T., *et al.* (2004) Expanded dynamic range of fluorescent indicators for Ca^{2+} by circularly permuted yellow fluorescent proteins, *Proc. Natl. Acad. Sci. U.S.A. 101*, 10554–10559.
6. Nguyen, A.-W., and Daugherty, P.-S. (2005) Evolutionary optimization of fluorescent proteins for intracellular FRET, *Nat. Biotechnol. 23*, 355–360.
7. Vinkenborg, J.-L., *et al.* (2007) Enhanced sensitivity of FRET-based protease sensors by redesign of the GFP dimerization interface, *ChemBioChem 8*, 1119–1121.
8. Yang, F., Moss, L.-G., and Phillips, G.-N., Jr.1996The molecular structure of green fluorescent protein, *Nat. Biotechnol. 14*, 1246–1251.
9. Palm, G..-J., *et al.* (1997) The structural basis for spectral variations in green fluorescent protein, *Nat. Struct. Biol. 4*, 361–365.
10. Ouyang, M., Sun, J., Chien, S., and Wang, Y.2008Determination of hierarchical relationship of Src and Rac at subcellular locations with FRET biosensors, *Proc. Natl. Acad. Sci. U.S.A. 105*, 14353–14358.
11. Zacharias, D.-A., Violin, J.-D., Newton, A.-C., and Tsien, R.-Y. (2002) Partitioning of lipid-modified monomeric GFPs into membrane microdomains of live cells, *Science 296*, 913–916.
12. Rizzo, M.-A., *et al.* (2006) Optimization of pairings and detection conditions for measurement of FRET between cyan and yellow fluorescent proteins, *Microsci. Microanal. 12*, 238–254.
13. Wang, Y., *et al.* (2005) Visualizing the mechanical activation of Src, *Nature 434*, 1040–1045.
14. Jost, C. A., Reither, G., Hoffmann, C., and Schultz, C. (2008) Contribution of fluorophores to protein kinase C FRET probe performance, *ChemBioChem 9*, 1379–1384.
15. Heim, N., *et al.* (2007) Improved calcium imaging in transgenic mice expressing a troponin C-based biosensor, *Nat. Methods 4*, 127–129.
16. Imamura, H., *et al.* (2009) Visualization of ATP levels inside single living cells with fluorescence resonance energy transfer-based genetically encoded indicators, *Proc. Natl. Acad. Sci. U.S.A. 106*, 15651–15656.
17. Carlson, H.-J., and Campbell, R.-E. (2009) Genetically encoded FRET-based biosensors for multiparameter fluorescence imaging, *Curr. Opin. Biotechnol. 20*, 19–27.
18. Goedhart, J., *et al.* (2007) Sensitive detection of p65 homodimers using red-shifted and fluorescent protein-based FRET couples, *PLoS ONE 2*, e1011.
19. Shcherbo, D., *et al.* (2009) Practical and reliable FRET/FLIM pair of fluorescent proteins, *BMC Biotechnol. 9*, 24.
20. Shimozono, S., *et al.* (2006) Concatenation of cyan and yellow fluorescent proteins for efficient resonance energy transfer, *Biochemistry 45*, 6267–6271.
21. Sawano, A., and Miyawaki, A. (2000) Directed evolution of green fluorescent protein by a new versatile PCR strategy for site-directed and semi-random mutagenesis, *Nucleic Acids Res. 28*, E78.
22. Kotera, I., and Nagai, T. (2008) A high-throughput and single-tube recombination of crude PCR products using a DNA polymerase inhibitor and type IIS restriction enzyme, *J. Biotechnol. 137*, 1–7.

Intracellular Calcium Spikes in Rat Suprachiasmatic Nucleus Neurons Induced by BAPTA-Based Calcium Dyes

Jin Hee [Hong][1], Cheol Hong [Min][1], Byeongha Jeong[1], Tomoyoshi Kojiya[2], Eri Morioka[2], Takeharu Nagai[3], Masayuki Ikeda[2], Kyoung J. Lee[1*]

1 Center for Cell-dynamics and Department of Physics, Korea University, Seoul, Republic of Korea,

2 Graduate School of Innovative Life Science, Toyama University, Toyama, Japan,

3 Laboratory for Nanosystems Physiology, Research Institute for Electronic Science, Hokkaido University, Sapporo, Japan

* E-mail: kyoung@korea.ac.kr

Background: Circadian rhythms in spontaneous action potential (AP) firing frequencies and in cytosolic free calcium concentrations have been reported for mammalian circadian pacemaker neurons located within the hypothalamic suprachiasmatic nucleus (SCN). Also reported is the existence of "Ca^{2+} spikes" (i.e., $[Ca^{2+}]_c$ transients having a bandwidth of 10 ~ 100 seconds) in SCN neurons, but it is unclear if these SCN Ca^{2+} spikes are related to the slow circadian rhythms.

Methodology/Principal Findings: We addressed this issue based on a Ca^{2+} indicator dye (fluo-4) and a protein Ca^{2+} sensor (yellow cameleon). Using fluo-4 AM dye, we found spontaneous Ca^{2+} spikes in 18% of rat SCN cells in acute brain slices, but the Ca^{2+} spiking frequencies showed no day/night variation. We repeated the same experiments with rat (and mouse) SCN slice cultures that expressed yellow cameleon genes for a number of different circadian phases and, surprisingly, spontaneous Ca^{2+} spike was barely observed (< 3%). When fluo-4 AM or BAPTA-AM was loaded in addition to the cameleon-expressing SCN cultures, however, the number of cells exhibiting Ca^{2+} spikes was increased to 13~14 %.

Conclusions/Significance: Despite our extensive set of experiments, no evidence of a circadian rhythm was found in the spontaneous Ca^{2+} spiking activity of SCN. Furthermore, our study strongly suggests that the spontaneous Ca^{2+} spiking activity is caused by the Ca^{2+} chelating effect of the BAPTA-based fluo-4 dye. Therefore, this induced activity seems irrelevant to the intrinsic circadian rhythm of $[Ca^{2+}]_c$ in SCN neurons. The problems with BAPTA based dyes are widely known and our study provides a clear case for concern, in particular, for SCN Ca^{2+} spikes. On the other hand, our study neither invalidates the use of these dyes as a whole, nor undermines the potential role of SCN Ca^{2+} spikes in the function of SCN.

Introduction

The circadian clock system governs various daily rhythms in physiological activities, from cellular autonomic activities to animal behaviors. The key component of this system is the suprachiasmatic nucleus (SCN) [1-3]. The SCN is composed of a pair of nuclei, each of which is comprised of 8,000 neurons approximately [4,5]. One key property of SCN neurons is the circadian oscillation in their spontaneous action potential (AP) firing rates [6-9]. Recent studies have shown that intracellular circadian oscillations are the result of transcription-translation feedback loops arising from multiple "clock genes" [1,10]. Yet, no one has shown how clock gene products modulate AP firing frequencies in SCN neurons.

The concentration of cytosolic free Ca^{2+} ions ($[Ca^{2+}]_c$) is a general intracellular messenger regulating a variety of different cellular processes, including membrane potentials and gene expression. Thus, it is possible that $[Ca^{2+}]_c$ is a mediator coupling clock gene oscillations and AP firing rhythms in SCN neurons [9,11-14]. Indeed, Colwell observed that the level of $[Ca^{2+}]_c$ was higher during day time than night time by using fura-2 [15]. Subsequently, a few years ago, one of us observed circadian rhythms in $[Ca^{2+}]_c$ of cultured mouse SCN neurons that expressed yellow cameleon, a Ca^{2+}-

sensing protein [14,16,17]. In the presence of tetrodotoxin, the AP firing activity of SCN disappeared completely but the circadian rhythm of $[Ca^{2+}]_c$ was persistent. On the other hand, the amplitudes of circadian oscillations, both in AP firing rate and $[Ca^{2+}]_c$, were significantly reduced by ryanodine and 8-bromo-cADP ribose. Thus, the release of Ca^{2+} from internal Ca^{2+} stores might have driven AP circadian oscillations in SCN neurons.

In addition to the slow circadian modulation of $[Ca^{2+}]_c$, there have been reports on Ca^{2+} spikes that have a duration in the order of several seconds to a minute in SCN neurons. For example, van den Pol et al. discussed SCN Ca^{2+} spikes in connection with neuro-glia interactions [18,19]. Their studies were based on fluo-3 and fura-2 imaging of cultured SCN cells. More recently, using patch pipettes filled with fura-2, Irwin and Allen demonstrated that electrical stimulation of retinohypothalamic tracts could evoke Ca^{2+} spikes [20]. They were strongly correlated with AP firing in SCN neurons. Also, Ikeda et al. observed spontaneous Ca^{2+} spikes in fura-2 stained acute SCN slices [21].

Knowing that SCN cells support two rather temporally distinct $[Ca^{2+}]_c$ dynamics, we investigated their relationship: In particular, we looked for the existence of circadian modulation in the Ca^{2+} spiking frequency. We also investigated the nature of spontaneous Ca^{2+} spikes in SCN based on two different Ca^{2+} indicators, fluo-4 dye and yellow cameleon.

Materials and Methods

Ethics Statement

All experimental procedures and protocols above were in accordance with the guidelines established by the Committee of Animal Research Policy of Korea University College of Medicine and Toyama University.

Acute Brain Slice Preparation

We used standard procedures to prepare acute brain slices containing SCN. More specifically, we used male Sprague-Dawley (SD) rats of 12-15 days old that had been bred under a 12:12 h light-dark cycle (lights on from 0800-2000) at a constant temperature (22~24°C). For the night time recordings, the animals were maintained in a reversed light-dark cycle (lights on from 2000-0800) for at least 2 weeks before the slice preparations. Once the rats had been deeply anesthetized with sodium pentobarbital (100 mg/kg body weight, i.p.), we prepared coronal hypothalamic slices (300 μm) containing the SCN with a vibratome (TPI, St. Louis, MO, USA) in ice-cold low-Ca^{2+} artificial cerebrospinal fluid (ACSF) containing (in mM) 124 NaCl, 4.0 $MgSO_4$, 3 KCl, 1.25 NaH_2PO_4, 26 $NaHCO_3$, 0.5 $CaCl_2$, and 10 glucose, being adjusted to 300

mosmol/kg with sucrose and saturated with 5% CO_2 and 95% O_2. Typically, two or three brain slices were cut per each preparation but only the slice containing the rostrocaudal center of the SCN was used for recording. Therefore, each brain slice represents one animal. For the nighttime recordings, the brain slices were prepared between zeitgeber time (ZT) 11 and ZT12 (i.e., within an hour before lights off). For both daytime and nighttime recordings, the brain slices were incubated for at least 1 hour in a chamber containing oxygenated low-Ca^{2+} ACSF (1.3 mM $MgSO_4$, 1 mM $CaCl_2$).

Organotypic Slice Cultures

The organotypic SCN slice cultures were made from 2- to 3-day-old SD rats or from C57BL/6J mice as described previously [16]. The brains were quickly excised and dropped into ice-cold, filter-sterilized, low-Ca^{2+} ACSF. Coronal hypothalamic slices containing the SCN were cut at 400 μm for rats or 350 μm for mice using a vibroslicer (World Precision Instruments, Sarasota, FL, USA) on a clean bench. We cut two or three sequential slices from the rostral to the caudal brain starting at the rostral end of the anterior commissure. These slices were transferred to a 0.40-μm filter cup (Millicell-CM, Millipore, Bedford, MA, USA), placed in a standard 6-well plate, and cultured

with 1 mL of medium that consisted of 50% Eagle's basal medium, 25% Earle's balanced salt solution, and 25% heat-inactivated horse serum, supplemented with 5 mg/mL glucose and 1:100 Glutamax (Invitrogen, Carlsbad, CA, USA). The cultures were maintained in a CO_2 incubator at 36°C and 5% CO_2. The culture medium was changed every 3-4 days. Only the slice culture that clearly shows the rostrocaudal center of the SCN was used for imaging.

Patch-Clamp Recording

After preparation, each acute SCN slice was transferred to a recording chamber and superfused continuously with warmed regular ACSF (1.3 mM $MgSO_4$, 2 mM $CaCl_2$, 25–30°C, pH 7.4) supplemented with gentamicin (50 mg/L) at a flow rate of 0.5 mL/min. The ACSF was continuously bubbled with 95% O_2/5% CO_2. The whole-cell patch recordings were taken from 1 to 6 h after the slice preparation. The patch micro-electrode (~2 μm tip diameter; ~5 MΩ resistance) was filled with a solution containing (in mM) 140 K-gluconate, 10 HEPES, 2 $MgCl_2$, 1 $CaCl_2$, 11 EGTA, 2 K_2ATP; (pH 7.3; osmolality 285–290 mosmol/kg) in accordance with methods described elsewhere [22]. The cell approach and the sealing were guided by series resistance changes monitored with current responses to the standard square voltage pulse. After successful contact had

been made between the micro-electrode and the target neuron, we applied a negative pressure to form a giga seal (2–5 GΩ). An additional gentle suction was used to disrupt the membrane and produce a whole-cell mode.

The membrane potential was measured continuously over 20 min in a current-clamp configuration using an Axoclamp 700A amplifier, a Digidata 1200 interface, and the pCLAMP 9.0 data acquisition/analysis software (Axon Instruments, Union City, CA, USA). The sampling rate was 10 kHz. The action potential peaks were detected by pCLAMP 9 data acquisition/analysis software, and the digitized data were analyzed Origin^{TM} ver.8.0 (OriginLab Co., Nortnampton, MA, USA) with custom-made programs.

Measurement of Intracellular Ca^{2+} Using Fluo-4

We used two different methods for fluo-4 dye loading into SCN neurons. First, we transferred acute SCN slices into a small home-built staining chamber and incubated them for 1 hr in oxygenated regular ACSF containing 20-μM fluo-4 acetoxymethyl ester (fluo-4 AM; Invitrogen), following the methods of Ikegaya et al. [23]. The stained slice was then transferred to a small recording chamber and washed for at least 20 min by perfusion of oxygenated regular ACSF in preparation for the subsequent imaging

experiment. This technique was used for the recording of multiple $[Ca^{2+}]_c$ responses from multiple cells in a single slice. We used the second method to make simultaneous measurements of $[Ca^{2+}]_c$ concentrations and membrane potentials in single SCN neurons, also by loading fluo-4 through patch micro-electrodes. The patch micro-electrodes were back-filled with an internal solution containing (in mM) 132 K-gluconate, 8 KCl, 8 NaCl, 10 HEPES, 0.5 $MgCl_2$, 4 Mg-ATP, and 0.4 Na-GTP (pH 7.3; osmolality 285–290 mosmol/kg) and filled with an internal solution containing fluo-4 pentapotassium salt (30-180 μM; Invitrogen) according to the methods described by Eilers and Konnerth [24]. Whole-cell current clamp recordings were taken as described above, and the SCN neurons were viewed with a laser-scanning confocal system (Fluoview 500, Olympus, Tokyo, Japan) attached to an upright microscope (BX51WI, Olympus) with a water immersion objective lens (Olympus UMPlanF1/10×/0.30W or LUMPlanF1 40×/0.8W). An argon laser (488 nm) was used for the excitation, and a green emission filter (515 ± 10 nm) was used to observe the fluorescent images. The series of image data was acquired and recorded by the Fluoview™ software package (Olympus). The fluorescent emission images were collected every 1.12 sec for a period of at least 18 minutes. Each image had a spatial resolution of 512 x 512 pixels. The relative fluorescent intensity change ($\Delta F = F - F_0$, where F_0 is the initial fluorescent

intensity at the cell body of the SCN neuron) was calculated in order to monitor $[Ca^{2+}]_c$ variations.

Measurement of Intracellular Ca^{2+} Using Yellow Cameleon

Yellow cameleon genes (YC3.6 [25]) linked to a neuron-specific enolase promoter (pNSE/YC) or to a cytomegalovirus promoter (pCMV/YC) were transfected into rat or mouse SCN cultures using a Helios Gene Gun system (Bio-Rad Laboratories, Hercules, CA, USA), as described in earlier work [16,17]. The technique involves coating small gold particles (0.6 μm, 5 mg) with vector-carrying YC genes (20 μg) according to the manufacturer's instructions and then blasting them into the slice cultures at days 7 or 8 *in vitro*.

We used two different imaging setups for the cameleon imaging. The primary setup was designed for Ca^{2+} imaging analysis at a high sampling rate. In this setup, images were acquired by an iXon EMCCD camera (Andor, Belfast, Northern Ireland, UK) mounted on an inverted microscope (IX71, Olympus) that was equipped with a 10× objective lens (LUCPlanFL, NA0.30, Olympus), a mercury arc lamp, and a Dual-view optical module (Optical-insights, Tucson, AZ, USA). For excitation we used a filter set (OI-05-Ex, Chroma Technology, Rockingham, VT, USA) that included an

excitation bandpass filter (436 ± 20 nm) and a dichroic mirror (455DCLP, Chroma). In order to minimize the photo-bleaching, two neutral-density filters (ND6, ND50, Olympus) were placed in the excitation light path as well. The fluorescent emission was separated by a dichroic mirror (505DCXR, Chroma) and two emission bandpass filters (480 ± 30 nm and 535 ± 40 nm) installed in the Dual-view module. An electromagnetic shutter (Vincent Associates, Rochester, NY, USA) was placed in front of the lamp house. The shutter control, image acquisition, and online image processing were coordinated by software based on the Andor SDK subroutine packages. A SCN slice that had successful YC expression was transferred to the recording chamber and superfused with warmed oxygenated regular ACSF. The fluorescent emission images were collected every 1.5 seconds for more than 5 minutes. The acquired images were further analyzed by ImageJ (NIH, Bethesda, Maryland, USA) with custom-built software.

The second imaging setup was based on the original cameleon imaging system created for the long-term monitoring of $[Ca^{2+}]_c$ levels in SCN neurons [16,17]. That setup uses an inverted fluorescent microscope (Axiovert 405M, Carl Zeiss) equipped with a custom-built microscope stage CO_2 incubator, a mercury arc lamp, an excitation filter (435.8 nm DF10, Omega Optical, Brattleboro, VT, USA), an excitation neutral density filter (ND.5, Omega Optical), a dichroic mirror (455DRLP, Omega Optical),

and a 20× objective lens (Plan-Neofluar 20×, NA0.5, Carl Zeiss). The two emission bandpass filters (480DF30 and 535DF25, Omega Optical) are switched by a filter changer wheel (C4312, Hamamatsu Photonics, Hamamatsu, Japan). We acquired the resulting image pairs through a cooled CCD camera (C6790, Hamamatsu) at a sampling rate of 1 frame per 3 seconds for detecting Ca^{2+} spikes or of 1 frame per 10 minutes for detecting circadian $[Ca^{2+}]_c$ oscillations. Argus-HiSCA imaging software (Hamamatsu) was used to control an electromagnetic shutter (Copal, Tokyo, Japan), a filter changer wheel, and image acquisition.

Statistical Analyses

Means were calculated along with standard errors. Single pairwise comparisons were analyzed with the two-tailed Student's t-test. A one-way analysis of variance (ANOVA) was used to compare the population percentage of differently prepared SCN slices and the different Ca^{2+} spiking responses to different levels of fluo-4 AM concentration.